

Toward High Conversion Efficiency of Thermoelectric Modules through Synergistical Optimization of Layered Materials

Wenjie Li,* Bed Poudel,* Ravi Anant Kishore, Amin Nozariasbmarz, Na Liu, Yu Zhang, and Shashank Priya*

Waste-heat electricity generation using high-efficiency solid-state conversion technology can significantly decrease dependence on fossil fuels. Here, a synergistical optimization of layered half-Heusler (hH) materials and module to improve thermoelectric conversion efficiency is reported. This is realized by manufacturing multiple thermoelectric materials with major compositional variations and temperature-gradient-coupled carrier distribution by one-step spark plasma sintering. This strategy provides a solution to overcome the intrinsic concomitants of the conventional segmented architecture that only considers the matching of the figure of merit (zT) with the temperature gradient. The current design is dedicated to temperature-gradient-coupled resistivity and compatibility matching, optimum zT matching, and reducing contact resistance sources. By enhancing the quality factor of the materials by Sb-vapor-pressure-induced annealing, a superior zT of 1.47 at 973 K is achieved for (Nb, Hf)FeSb hH alloys. Along with the low-temperature high- zT hH alloys of (Nb, Ta, Ti, V)FeSb, the single stage layered hH modules are developed with efficiencies of $\approx 15.2\%$ and $\approx 13.5\%$ for the single-leg and uncouple thermoelectric modules, respectively, under ΔT of 670 K. Therefore, this work has a transformative impact on the design and development of next-generation thermoelectric generators for any thermoelectric material families.

is focused on developing technologies that can convert heat into electricity with high efficiency. Thermoelectric generators (TEGs) can directly convert waste heat into electricity via the Seebeck effect.^[1] The conversion efficiency (η) of a thermoelectric (TE) device is governed by

$$\eta = \frac{T_h - T_c}{T_h} \frac{\sqrt{1 + zT_{\text{avg}}} - 1}{\sqrt{1 + zT_{\text{avg}}} + T_c/T_h} \quad (1)$$

where zT_{avg} is the average figure of merit of TE materials, and ΔT ($T_h - T_c$, where T_h and T_c are the hot- and cold-side temperatures, respectively) is the temperature gradient across the device. The TE properties, including the electrical resistivity (ρ), Seebeck coefficient (α), and thermal conductivity (κ), determine the material's figure of merit (zT), as follows

$$zT = \alpha^2 T / \rho \kappa \quad (2)$$

These properties are dependent on the carrier concentration (n_{H}) and carrier mobility (μ_{H}).^[2]

Tremendous efforts have focused on improving the zT of various materials for different operating temperatures.^[3–11] Among TE materials, half-Heusler (hH) alloys have promising zT ,^[8,12,13] stability,^[14,15] and mechanical strength^[16] at 773–1073 K. Recently, NbFeSb-based p-type hH alloys exhibit a high peak zT realized by solid solution,^[13] band degeneracy,^[17] and hierarchical design^[18] approaches. With the improvements in hH materials, module performance has been increasing in the past decade.^[19–21] In particular, single-stage hH-based modules can reach a conversion efficiency of up to 10–11%.^[8,20] However, further improvements in the module efficiency are limited by the low zT_{avg} of hH alloys.


To achieve a high zT_{avg} and large temperature gradient across TE legs, segmented TE modules using BiTe-based materials as the low-temperature stage, and materials, such as lead telluride, skutterudite, and hH alloys for medium- and high-temperature stages have been developed. However, this approach can only slightly promote the maximum conversion efficiency (η_{max}) by up to $\approx 12\%$ ^[22–24] owing to several intrinsic concomitant factors from the conventional segmentation design. First, the large difference in the densification temperatures between the materials used in the segmented legs imposes restrictions on sintering them together. Hence, the segments in the TE legs must be

1. Introduction

The increasing global demand for energy has accelerated the development of energy-harvesting technologies that can generate electricity from available energy sources. Waste heat is one of the most common energy sources; thus, significant interest

W. Li, B. Poudel, A. Nozariasbmarz, N. Liu, Y. Zhang, S. Priya
Department of Materials Science and Engineering
Pennsylvania State University
University Park, PA 16802, USA
E-mail: wzl175@psu.edu; bup346@psu.edu; sup103@psu.edu

R. A. Kishore
National Renewable Energy Laboratory
15013 Denver West Pkwy, Golden, CO 80401, USA

 The ORCID identification number(s) for the author(s) of this article can be found under <https://doi.org/10.1002/adma.202210407>.

© 2023 The Authors. Advanced Materials published by Wiley-VCH GmbH. This is an open access article under the terms of the Creative Commons Attribution-NonCommercial-NoDerivs License, which permits use and distribution in any medium, provided the original work is properly cited, the use is non-commercial and no modifications or adaptations are made.

DOI: 10.1002/adma.202210407

soldered or brazed using heterogeneous joint materials to form a segmented architecture, thereby generating heterogeneous interfaces, external electrical and thermal contact resistance, and weak mechanical properties. Second, the segments have a large resistivity difference. The load current passing through the entire segmented TE leg leads to a resistivity mismatch among the segments, which implies that different materials cannot be operated under optimum conditions. This results in a performance lower than the expected outcome from the combination of different material segments. Third, according to the compatibility factor (s) theory,^[25] the difference in the optimum relative current density (u) among the segments restricts their efficient operation in a specific current magnitude. As the difference in s between these materials is higher than 2,^[26] the performance of the segmented devices is below expectations.

Functionally graded materials (FGMs) are materials with gradual variations in their compositions, structures, or properties throughout their volume. It can be either interconnecting of more than one segments/layers or continuously grading the compositions. Functionally graded doping is to introduce doping in each segment of the sample that is optimized for the operating temperature gradient for that piece.^[27] Module performance has been enhanced using FGMs with appropriate geometrical optimization, such as in Sb_2Te_3 , $\text{Mg}_3(\text{Sb}, \text{Bi})_2$, PbTe , and Bi_2Te_3 systems for low- and medium-temperature power generation.^[28–32] In conventional FGMs, only minor compositional variants are deployed to vary the TE properties, which restrict their applications. Contact electrode material, such as Ni, has been widely used to fabricate conventional FGMs.^[31,32] However, it can introduce heterogeneous interfaces, interdiffusion between the electrode and TE materials, and a mismatch between the coefficient of thermal expansion (CTE). Previously, we developed a direct bonding technique for hH TE devices, which demonstrated negligible contact resistance and clear interface, thereby achieving good TE performance with thermal

stability.^[19] Nonetheless, the aforementioned issues should be synergistically addressed through a layered material and device design.

In this study, we demonstrate a synergistically optimized layered architecture obtained by a direct bonding technique on hH alloys with major compositional variants. A spatially distributed electrical conductivity and Seebeck coefficients with optimum temperature gradients across each material were obtained to overcome resistivity and compatibility mismatch issues, and avoid heterogeneous interfaces, while maintaining high zT_{avg} . To implement this, we synthesized MFeSb ($M = \text{Nb}, \text{Ta}, \text{Ti}, \text{V}, \text{Hf}$) hH alloys, which exhibit high zT at 298–683 K ($\text{Nb}_{0.45}\text{Ta}_{0.4}\text{V}_{0.1}\text{Ti}_{0.05}\text{FeSb}$, denoted as TaV) with a low carrier concentration, and $\text{Nb}_{0.88}\text{Hf}_{0.12}\text{FeSb}$ alloys, marked as NbHf, which exhibit high zT between 683 and 973 K with a high carrier concentration (Figure 1a). The NbHf alloy synthesized through the pressure-induced annealing (PIA) process has a high carrier concentration (low resistivity), low Seebeck coefficient, and distinguished peak zT of 1.47 at 973 K (Figure 1a). Subsequently, a synergistically optimized layered architecture with NbHf and TaV as the high- and low-temperature layers, respectively, was fabricated by one-step spark plasma sintering (SPS) of the p-type hH leg. Based on the performance of the advanced material, the optimized geometric dimensions of the TE material were calculated following previously reported concise module design^[24] to couple the temperature profile, resistivity, and Seebeck coefficient with a temperature gradient. As a result, the state-of-the-art conversion efficiencies of $\approx 15.2\%$ for a single leg and $\approx 13.5\%$ for the uncouple module at ΔT of 670 K were obtained (Figure 1b), which are the highest values reported for single-leg and π -type TE modules.^[8,20,22–24,33–39] This result can be ascribed to three aspects: superior material performance, temperature-coupled resistivity and compatibility matching, and extremely low contact resistance. The strategy of current design is further summarized in Figure S1 (Supporting Information).

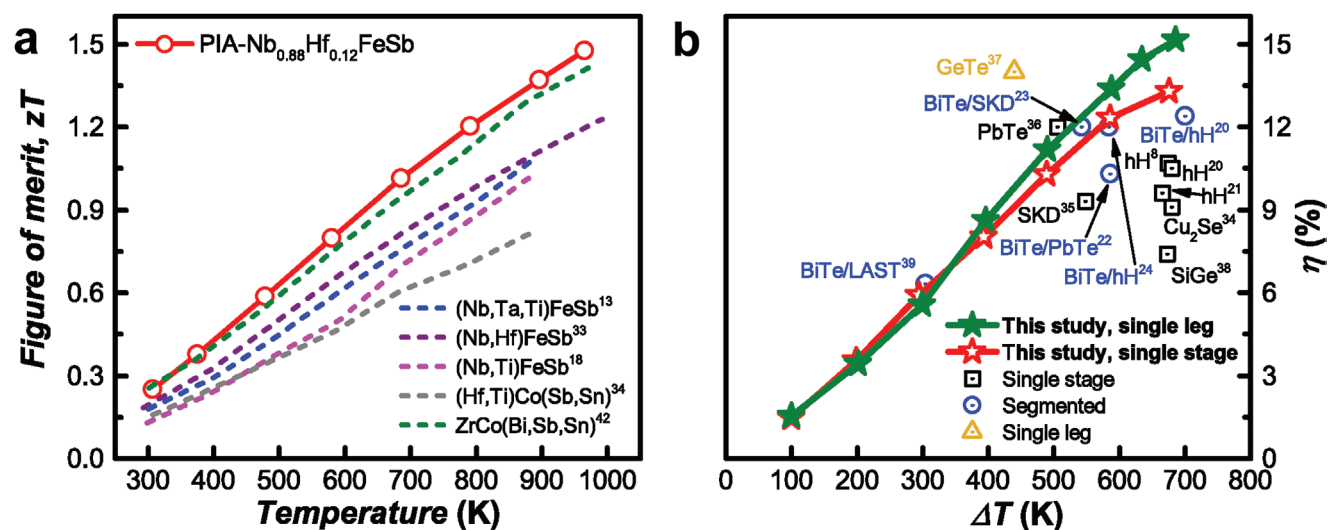


Figure 1. Figure of merit (zT) of p-type hH alloys and conversion efficiency of TE modules, compared to reported results.^[13,18,40–42] a) zT of hH materials as a function of temperature. b) Conversion efficiency of the synergistically optimized layered hH TE modules as a function of the temperature gradient (ΔT).

2. Results and Discussion

2.1. Synergistical Optimization of Layered hH Architecture

The conventional segmentation design attempts to maximize only zT_{avg} and ΔT . However, it simultaneously introduces resistivity, compatibility mismatch, and heterogeneous interfacial contact resistance. Meanwhile, the transport properties of materials are not considered as a function of the temperature gradient along the device, which further leads to the nonoptimum performance for each segment.^[43] The synergistically optimized layered hH design with different dopants based on $(\text{Nb}_x\text{M}_{1-x})\text{FeSb}$ ($x = 0.45$ and 0.88) compositions, where M-site is occupied by either dopant of Hf when $x = 0.88$ or $(\text{Ta}_{0.73}\text{V}_{0.18}\text{Ti}_{0.09})$ when

$x = 0.45$, is demonstrated. More than two layers can be interconnected, as illustrated in Figure 2a (two layers) and Section S2 (multiple layers) (Supporting Information), fully accounting for the properties of various materials and interfacial engineering. First, compositional layers from the same material system (e.g., hH) were stacked with high to low carrier concentrations along the temperature gradient. Consequently, the gradient TE properties, including resistivity and Seebeck coefficient, can be coupled with the temperature gradient. Thus, TE materials with various compositions can be fabricated through a direct bonding technique by one-step SPS to eliminate the heterogeneous interface, thereby reducing the contact resistance. In addition, as the leg is fabricated using compositions of the same materials, the CTE mismatch between these layers

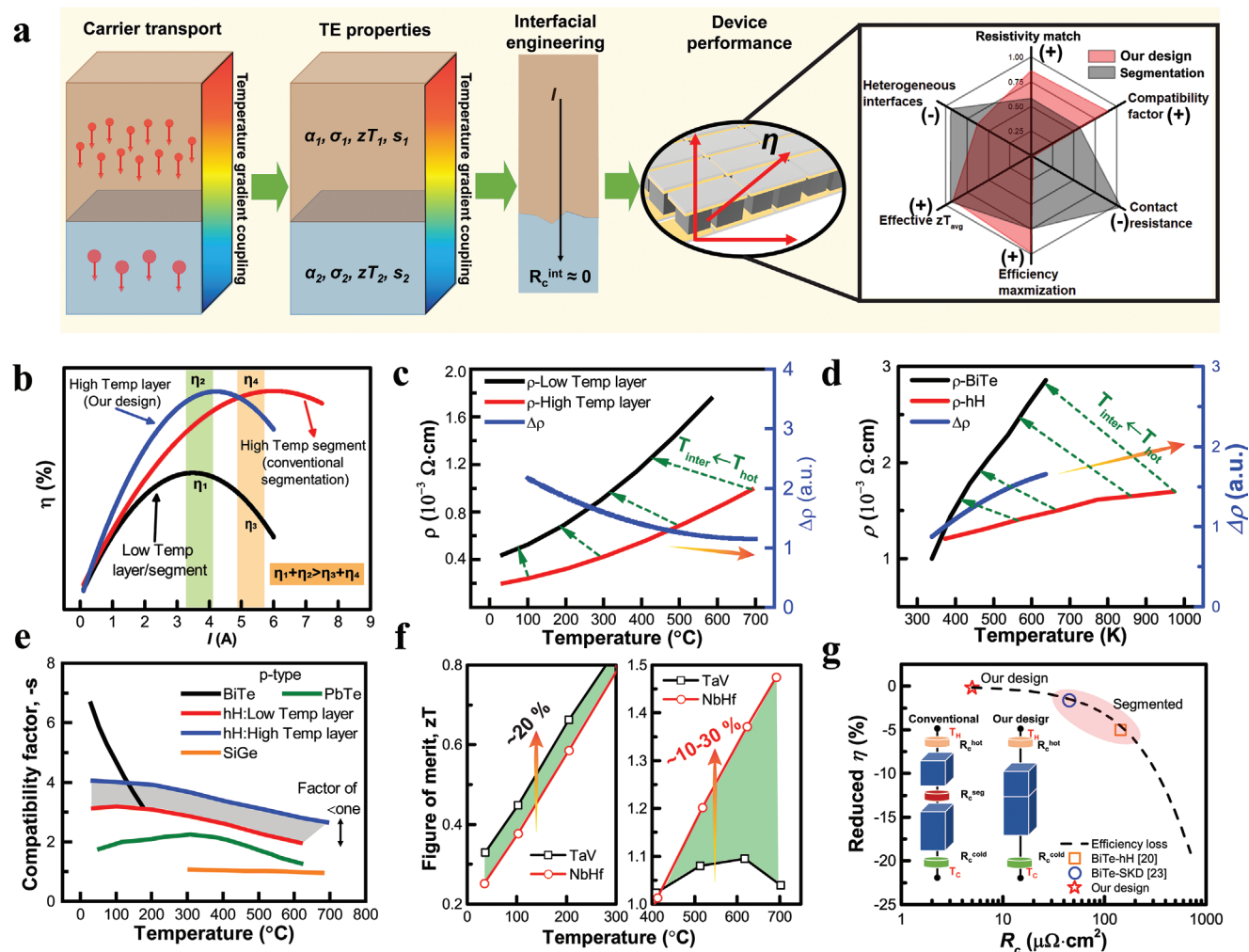


Figure 2. Synergistical optimization of layered architecture design. a) Synergistically optimized layered design, and comparison of the features with conventional segmentation. R_c^{int} is the contact resistance at the interfaces. Definition, metrics, and values in the hexagonal radar are summarized in Table S1 (Supporting Information), where the calculations are based on the experimental results of NbHf and TaV p-hH compositions and our previous work on BiTe/hH segmentation.^[24,48] The (+) and (-) signs indicate the positive and negative impacts on the enhancement of η with increased values in these terms, respectively. b) Conversion efficiency (η) for synergistically optimized layered design (green, $\eta_1 + \eta_2$) and conventional segmentation (yellow, $\eta_3 + \eta_4$) design. c,d) Resistivity matching ($\Delta\rho$) in conventional BiTe-hH segmentation (c) and synergistically optimized layered (d) p-type materials.^[24] e) Compatibility factor (s). f) zT of TaV and NbHf in their optimum temperature range. g) Effect of contact resistance on the efficiency loss.^[20,23] The inset shows a schematic of the contact resistance sources in conventional segmentation and synergistically optimized layered design. T_h and T_c represent the hot and cold sides, respectively; R_c^{hot} , R_c^{seg} , and R_c^{cold} are contact resistance at the interfaces. The details of the synergistically optimized layered design and compatibility factor are described in Figures S2 and S3 and Table S1 (Supporting Information).

is significantly reduced, resulting in more stable devices and a more similar compatibility factor to produce higher conversion efficiency. Therefore, in addition to achieving optimal zT in different temperature ranges, the synergistically optimized layered architecture can achieve resistivity and current density matching by coupling the charge transport properties with a temperature gradient to improve the device performance.

The η_{\max} of the TEGs was achieved when the applied external load was identical to the internal resistance. In the conventional TE segmentation design, where an identical current passes through the TE leg, the resistivity difference ($\Delta\rho$) between the materials was large because different material systems, such as BiTe, skutterudite (SKD), PbTe, and hH, were employed. The total conversion efficiency of the device, $\eta_3 + \eta_4$ (Figure 2b), is between the values for each segment as a trade-off efficiency ($\eta_{\text{trade-off}}$) because each segment stage cannot achieve its η_{\max} under the same current. For instance, $\Delta\rho$ increased in conventional BiTe–hH segmentation at elevated temperatures, where the resistivity of the BiTe segment is almost twice that of the hH segment at the desired high operational temperature. Thus, the trade-off effect of the efficiency increased at elevated temperatures, leading to a low $\eta_{\text{trade-off}}$ (Figure 2c). In this study, the same material system was utilized to achieve a close $\Delta\rho$ matching between two hH materials. As shown in Figure 2d, the $\Delta\rho$ values of TaV and NbHf are closer at elevated temperatures and are almost equal at the desired high operational temperature (NbHf at ≈ 973 K and TaV at ≈ 673 K), leading to a high η_{\max} . Thus, the uniqueness of the synergistical optimization of layered architecture can simultaneously achieve the optimum efficiency for both segments, which is $\eta_1 + \eta_2 > \eta_3 + \eta_4$ (Figure 2b).

Compared to the current design, the normalized efficiency loss from conventional segmentation is $\approx 25\%$ (Table S1, Supporting Information). Theoretically, the change in the compatibility factor of the segmented materials should be limited to a factor of two to achieve a high η_{\max} ,^[26] which is an inevitable challenge for conventional segmentation (Figure 2e and Section S3 (Supporting Information)). Our synergistically optimized layered design provides two hH compositions with a compatibility difference of less than one for the entire temperature range, thereby further increasing η_{\max} . TaV and NbHf alloys have superior zT performance in the range of 298–683 and 683–973 K, respectively. The zT of TaV is $\approx 20\%$ higher than that of NbHf below 573 K, whereas that of NbHf is up to $\approx 30\%$ higher than that of TaV above 673 K (Figure 2f). Thus, the effective zT_{avg} significantly increased in the design, which can enhance the conversion efficiency of the TE module by 30–40%, compared to single-stage NbHf or TaV modules. The temperature at the TaV/NbHf interface was designed to be the crossover temperature of zT to allow the materials to operate in their optimum temperature range (Figure 2f).

The heterogeneous interfacial contact resistance is an unavoidable problem in conventional segmentation. The device zT (zT_d) is defined as

$$(zT)_d = (zT)_m \times \left(\frac{L}{L + 2R_c\sigma} \right) \quad (3)$$

where $(zT)_m$, L , R_c , and σ are the material zT , TE leg height, contact resistance, and electrical conductivity, respectively. The

total contact resistance of the device (R_c^{total}) is the sum of that of the individual interfaces as follows

$$R_c^{\text{total}} = R_c^{\text{hot}} + R_c^{\text{cold}} + R_c^{\text{seg}} \quad (4)$$

where R_c^{hot} , R_c^{cold} , and R_c^{seg} are the contact resistance between the hot-side and cold-side of the TE legs and electrode, and between the segments, respectively (Figure 2g). The electrical and thermal contact resistances were in the ranges of 1×10^{-9} – $1 \times 10^{-7} \Omega \text{ m}^2$ and 1×10^{-6} – $1 \times 10^{-4} \text{ m}^2 \text{ K}^{-1} \text{ W}^{-1}$, respectively.^[44,45] Ouyang and Li^[46] demonstrated that the conversion efficiency could be reduced by $\approx 85\%$ and 37% with an increase in the electrical and thermal contact resistances, respectively. Although different soldering/brazing materials have been explored to minimize contact resistance,^[20,23,24,47] the electrical and thermal contact resistances can still decrease the device performance, especially for upscaled devices for practical applications.^[21] In this study, the layered hH alloys were manufactured by one-step SPS through a direct bonding technique, which eliminated heterogeneous interface, thereby significantly reducing the contact resistance (Figure 2g). The η loss in the conventional segmentation module was $\approx 5\%$, which was significantly higher than that of our synergistically optimized layered design ($\approx 0.2\%$). The η loss is higher considering the thermal contact resistance from the heterogeneous interface in conventional segmentations.

The hexagonal radar provides a comprehensive comparison between the synergistically optimized layered design and conventional segmentation, illustrating the advantage of the former for a higher TE performance. A two-layers synergistically optimized architecture of hH materials is demonstrated. The TE efficiency can be potentially further improved when multilayer materials that fit the criteria are realized (Figure S2, Supporting Information), which can be realized by various TE materials.

2.2. Chemical Defects by PIA

Defect engineering serves as a scaffold to tailor TE parameters by manipulating the behavior of intrinsic electrons and phonon, thereby enhancing the power factor and reducing the lattice thermal conductivity.^[49] Wood et al. developed a Mg-vapor annealing process to compensate for Mg loss in a high-temperature treatment process, thereby maintaining a high n-type carrier concentration.^[50] In the MFeSb matrix (M: transition metal), Sb has a low vapor pressure and can be volatilized at elevated temperatures. This provides a promising approach to manipulate chemical defects, thereby enhancing TE properties. Thus, a Sb-site vapor PIA was developed in this study to simultaneously reduce the lattice thermal conductivity and improve the power factor (Figure S4, Supporting Information).

The total (κ_{total}) and lattice (κ_{lattice}) thermal conductivity (calculation in the Supporting Information) decreased from ≈ 3.84 to ≈ 3.2 and from ≈ 2.3 to $\approx 1.59 \text{ W m}^{-1} \text{ K}^{-1}$, respectively, as the PIA temperature was increased to 973 K (Figure 3a). This represents a reduction of 6–15% in the as-synthesized material. The increased substitutional defects introduced by strong mass and strain fluctuations can reduce the lattice thermal conductivity.^[37,51] The alloying-induced lattice strains can be derived

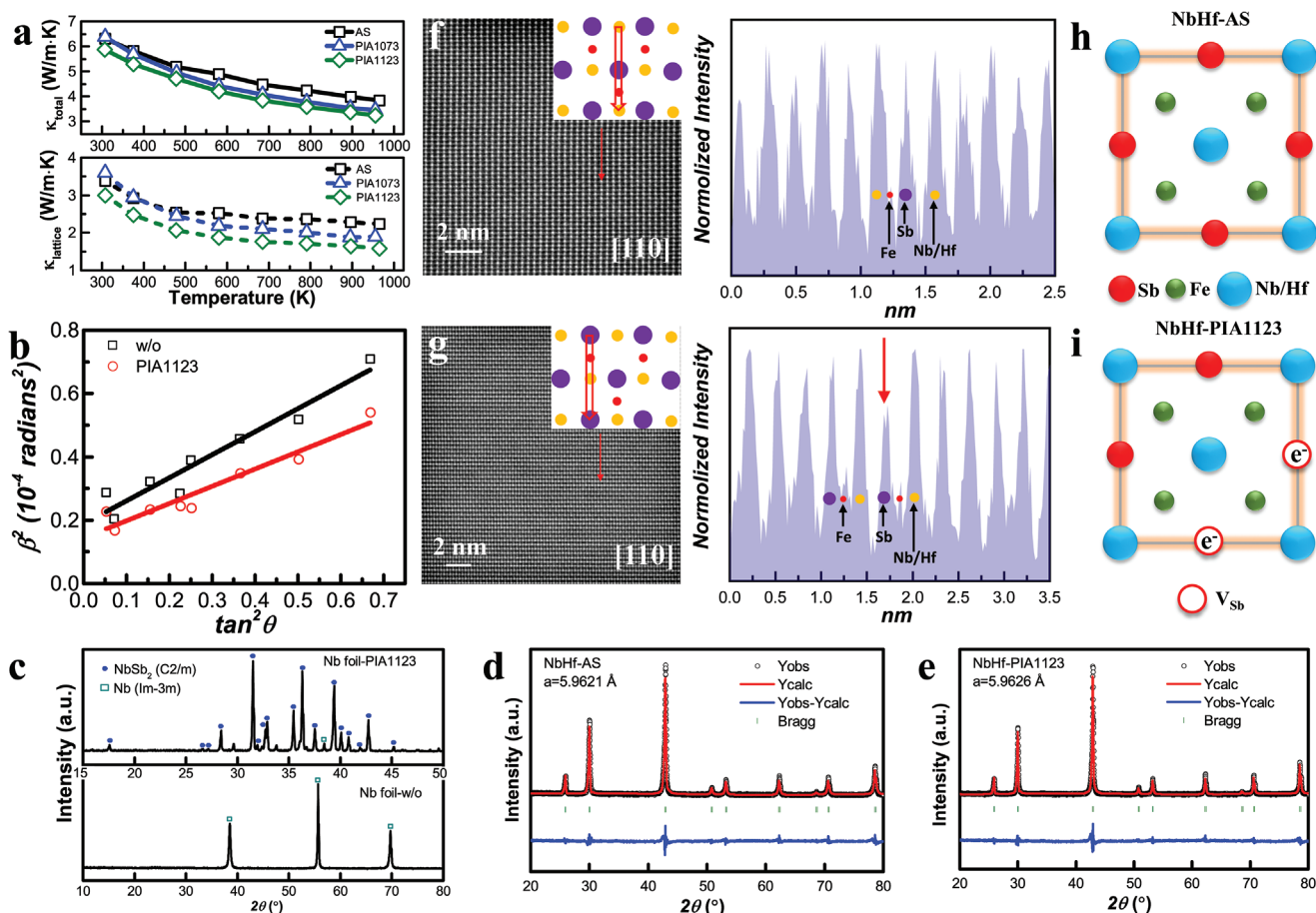


Figure 3. Thermal transport and figure of merit of NbHf. a) Total (κ) and lattice (κ_L) thermal conductivity of NbHf-AS, NbHf-PIA1073, and NbHf-PIA1123. b) Lattice strain analysis for NbHf-AS and NbHf-PIA1123. The intercept and slope of the linear fit illustrate the strain contribution of the grain boundaries and substitutional defects, respectively. c) XRD patterns of the Nb foil before (Nb foil-w/o) and after PIA at 1123 K (Nb foil-PIA1123). d, e) Rietveld refinement analysis of NbHf-AS (d) and NbHf-PIA1123 (e). Detailed results of the Rietveld refinement analysis are summarized in Table S2 (Supporting Information). f, g) HAADF-STEM image and intensity-scan profile along the [110] zone axis of NbHf-AS (f) and NbHf-PIA1123 (g). h, i) Sb-vacancy generation for NbHf-AS (h) and NbHf-PIA1123 (i).

from broadening the full width at half maximum (marked as β) in the X-ray diffraction (XRD) peaks, as shown in Figure 3b. The as-synthesized NbHf (NbHf-AS) and PIA-processed sample at 1123 K (NbHf-PIA1123) show a similar microstrain contribution from the substitutional defects. A slightly lower microstrain contribution was noted from the grain boundaries for the NbHf-PIA1123 sample, which can be ascribed to the microstrain released during PIA. This indicates that other mechanisms dominate the significant reduction in the lattice thermal conductivity of NbHf-PIA1123. The XRD pattern of the Nb foil used for PIA exhibits a major NbSb₂ phase (Figure 3c).

The Rietveld refinement results show reduced Sb occupancies for NbHf-PIA1123 (Figure 3d,e and Table S2 (Supporting Information)), indicating the off-stoichiometry of Sb. Figure 3f,g shows the high-angle annular dark-field scanning transition electron microscopy (HAADF-STEM) images obtained from the [110] zone axis with the intensity-scan profiles of NbHf-AS and NbHf-PIA1123. Compared to the uniform contrast of the Sb-site columns for NbHf-AS,

the unambiguous intensity contrast at the Sb-site indicated by the red arrow for NbHf-PIA1123 illustrates the existence of Sb-vacancies after PIA, which is consistent with the XRD analysis. This suggests that PIA initiated Sb evaporation owing to its low vapor pressure, thereby generating Sb-vacancies (Figure 3h,i and Section S4 (Supporting Information)). Several HAADF-STEM images were measured and analyzed from different areas of prepared sample. The reduced column intensity on Sb-site was observed consistently indicating the statistical significance of Sb-vacancy in NbHf-PIA1123 sample (Figure S5, Supporting Information). The electrons generated by the Sb-vacancies lowered the carrier concentrations, as confirmed by the Hall measurements (Table S3, Supporting Information). The relative density of NbHf-PIA slightly decreased from 99% to 95%, which is still very high and comparable to that of polycrystalline SnSe (Figure S7, Supporting Information),^[52] thereby contributing to phonon scattering.^[53] In addition to the local mass fluctuations of Nb and Hf, these defects play an important role in phonon scattering of phonons, resulting in reduced lattice thermal conductivity.

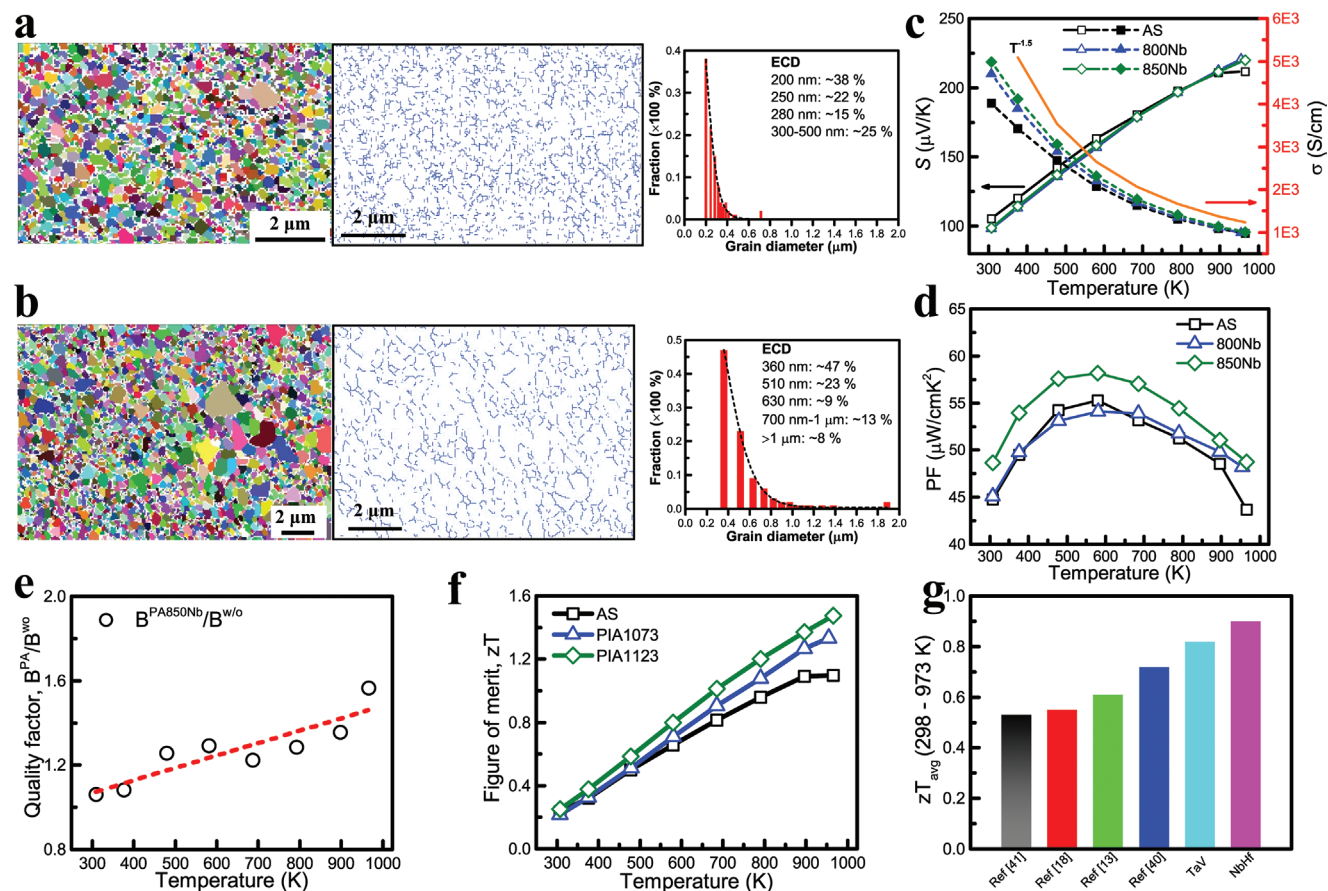


Figure 4. Electrical transport properties and EBSD analysis of NbHf. a, b) EBSD analysis of NbHf-AS and NbHf-PIA1123, showing their grain boundaries and size distributions. The grain boundaries are generated by the Oxford Aztec Crystal software, where the disconnected lines along grain boundaries are resulted from the ultrafine nanograins leading to a fraction of $\approx 15\%$ zero-solution regions during the EBSD analysis. ECD stands for the equivalent circle diameter. The different regions of the sample were investigated to illustrate similar grain size distributions. c, d) Seebeck coefficient (S) and electrical conductivity (σ), and power factor (PF) of the as-synthesized NbHf (NbHf-AS) and PIA-processed samples at 1073 K (NbHf-PIA1073) and 1123 K (NbHf-PIA1123) as a function of temperature. The marked regions indicate the enhancement of the electrical conductivity and PF. e) Quality factor ratio between the NbHf-AS and NbHf-PIA1123 samples as a function of temperature. f) Figure of merit of NbHf-AS, NbHf-PIA1073, and NbHf-PIA1123. g) zT_{avg} at 298–973 K of NbHf-PIA1123, compared to state-of-the-art results.^[13,18,40,41]

2.3. Grain Boundary Engineering and Quality Factor

The thermally activated resistivity (ρ_T) is described as follows^[54]

$$\rho_T = \frac{\rho_{gb}}{d} e^{-\frac{\Delta E}{k_B T}} \quad (5)$$

where ρ_{gb} , d , and ΔE are the effective grain-boundary resistance, grain size, and effective activation energy, respectively. Previous studies on TE alloys have focused on fine nanostructures to lower lattice thermal conductivity. The high grain boundary resistance and small grain size can be attributed to high ρ_T , resulting in the high κ_{total} and compromised power factor, particularly in the low- and medium-temperature ranges.^[54] Therefore, well-controlled grain growth is desirable to enhance the power factor while retaining the low thermal conductivity.

As shown in **Figure 4a,b**, the doubled grain size (NbHf-AS: 200–500 nm; NbHf-PIA1123: 400–1400 nm) with significantly reduced grain boundaries after the PIA process can significantly reduce electron scattering. Consequently, the electrical conductivity of the NbHf-PIA samples was improved. In par-

ticular, the electrical conductivity increased from ≈ 4000 to ≈ 5000 S cm^{-1} with the increase in the PIA temperature of up to 1123 K from room temperature, which follows a $T^{-1.5}$ trend that illustrates an acoustic-dominated scattering mechanism (Figure 4c). The Seebeck coefficient remained similar across the entire temperature range. Therefore, the power factor of NbHf-PIA1123 sample increased by $\approx 15\%$ and reached a maximum of ≈ 60 $\mu\text{W cm}^{-1} \text{K}^{-2}$ (Figure 4d). This did not significantly weaken the phonon scattering because more than 70% of the grains of NbHf-PIA1123 were still less than 500 nm (and 90% were less than 800 nm). Moreover, the good mechanical strength of the alloys was maintained (Figure 4c,d).

The quality factor B , which is proportional to $\approx \mu_w / \kappa_L$, was recently defined to guide the enhancement of TE materials by considering the reduction in κ_L and effect of weighted mobility (μ_w).^[55] Owing to the correlation of the TE parameters, an increase in B suggests an improved TE performance of the materials. In the simple free-electron model, μ_w can be described as

$$\mu_w = \mu (m_d^*)^{3/2} \quad (6)$$

where μ is the carrier mobility, and m_d^* is the density of the state effective mass (defined as m^*/m_e , where m^* and m_e are the effective and electron mass, respectively). The ratio of B among different samples can then be described as (see the Supporting Information)

$$\frac{B^i}{B^j} = \frac{\kappa_L^j}{\kappa_L^i} \cdot \frac{\mu^i}{\mu^j} \cdot \frac{n_H^i}{n_H^j} \cdot \left(\frac{\alpha^i}{\alpha^j}\right)^{3/2} \quad (7)$$

The $B^{\text{PIA1123}}/B^{\text{AS}}$ ratio has a similar value at room temperature but increases linearly up to ≈ 1.5 with increasing temperature at 973 K (Figure 4e). Thus, zT of NbHf-PIA1123 was significantly improved at 973 K, compared to that of NbHf-AS. The simultaneously improved power factor and reduced thermal conductivity achieved a remarkable zT of 1.47 at 973 K and zT_{avg} of 0.88 at 298–973 K for NbHf-PIA1123. This result exhibits a significant improvement, compared to state-of-the-art results (Figures 1a and 4g). For comparison, we also annealed NbHf in vacuum, whereby the TE performance of the materials was lower (Figure S9, Supporting Information). This strongly illustrates that the PIA process is crucial for the simultaneous optimization of electron and phonon transports, resulting in an enhanced zT performance.

2.4. Interface of Layered TaV–NbHf Material

In this study, we developed a TaV composition as a low-temperature layer. The TE properties of the TaV composition are summarized in Figure S11 (Supporting Information). The thickness of each layer was calculated using a concise design approach

to satisfy the temperature gradient requirement.^[24] The p-hH counterpart was processed by the one-step SPS of the TaV composition as the low-temperature layer and NbHf composition as the high-temperature layer, followed by PIA at 1123 K for three days to improve the TE performance and reach the equilibrium state of the material at the interface (Figure S12, Supporting Information). The elemental distribution of Nb in the NbHf composition and Ta in the TaV composition greatly varied, indicating the negligible diffusion between the two materials after reaching the equilibrium state (Figure 5a). The temperature of the PIA process at 1123 K was ≈ 450 K higher than the maximum operational temperature at the TaV–NbHf interface (≈ 673 K). Therefore, the interdiffusion at the TaV–NbHf interface during module operation is thermodynamically unfavorable.

Both layers exhibited randomly oriented grains, and a distinct phase boundary between TaV and NbHf from the electron backscattering diffraction (EBSD) phase analysis (Figure 5b–d). Kernel average misorientation calculations are widely used to map residual plastic strains.^[56] Because of the similar lattice parameters (TaV: 5.9626 Å, NbHf: 5.9413 Å) and PIA process, no obvious local plastic strains were observed at the interface, indicating excellent bonding strength (Figure 5c). The TE device performance was also determined by the ability to minimize the contact resistance, which is a challenge for conventional segmentation owing to the existence of a heterogeneous interface. A negligible electrical contact resistance of $<1 \mu\Omega \text{ cm}^2$ was achieved at the interface of the TaV–NbHf leg (Figure 5e), which is significantly lower than that of the conventional segmentations with contact resistances larger than $20 \mu\Omega \text{ cm}^2$.^[20,23,24,57]

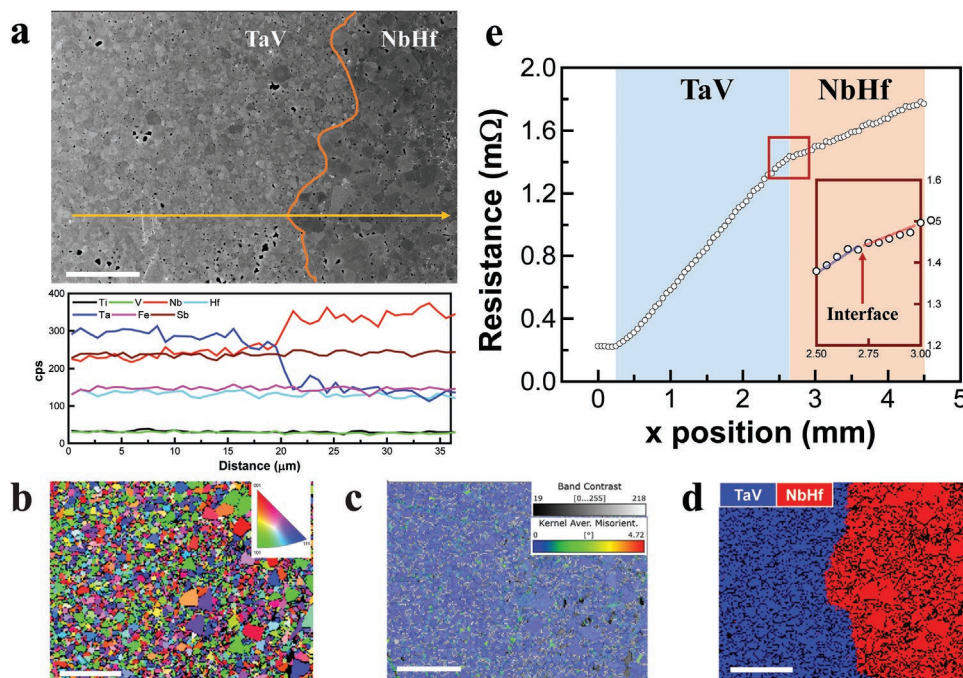


Figure 5. Interface of the TaV–NbHf materials fabricated by one-step SPS. a) SEM image, EDS line scan. The orange dashed line indicates the interface. b) Grain orientation of the EBSD images across the interface. c) Local microstrain analysis based on the Kernel average misorientation map. d) Phase analysis results obtained from EBSD using TruPhase function. The lattice parameters of 5.9626 Å (TaV) and 5.9413 Å (NbHf) obtained from Rietveld refinement are used. e) Contact resistance scan of the TaV–NbHf TE leg. The scale bars are 5 μm .

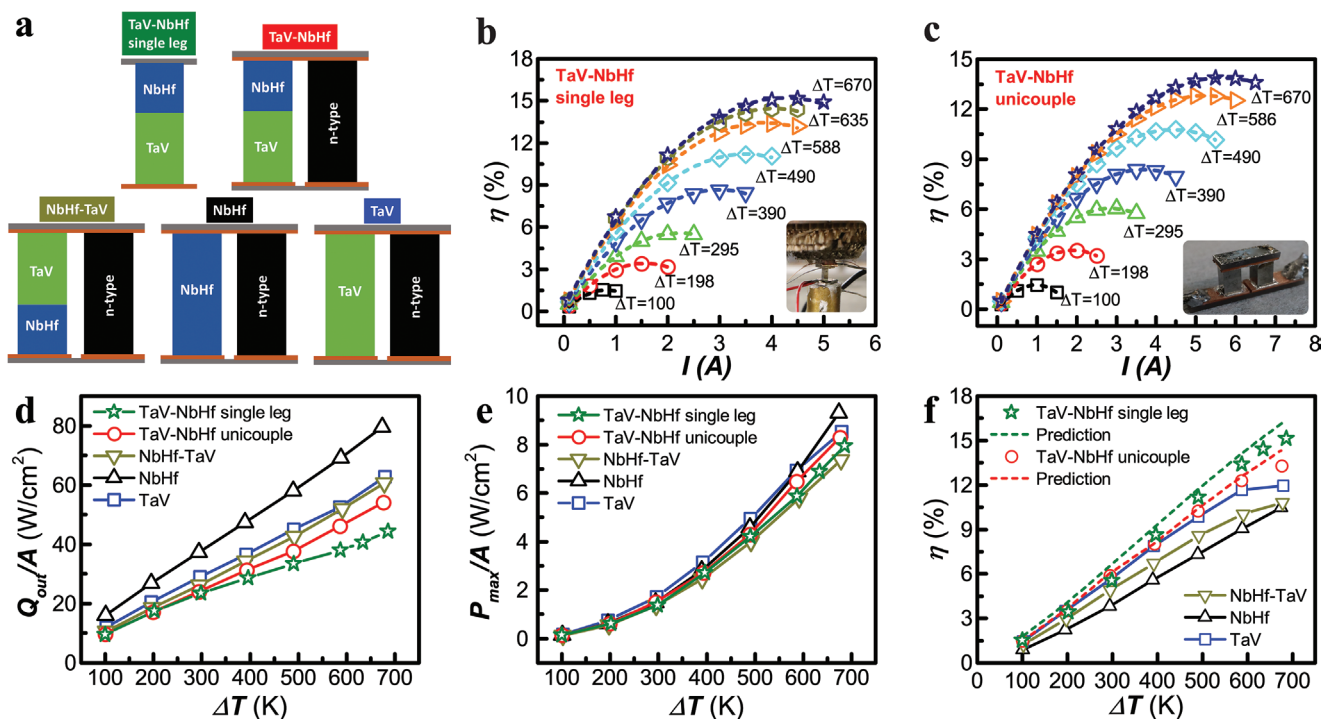


Figure 6. TE uncouple modules performance. a) Configurations of the TaV–NbHf single-leg modules and four uncouples, including TaV–NbHf, NbHf–TaV, TaV single, and NbHf single modules. b, c) Current-dependent conversion efficiency (η) of the TaV–NbHf single leg (b) and uncouple (c). d, e) Ratio of the heat flux on the Q-meter (Q_{out}) and output power (P_{max}) with the cross-sectional area of the TE leg (A) as a function of ΔT . f) Conversion efficiency (η) of the modules with five configurations shown in (a) under different ΔT .

2.5. TE Module Performance

The conversion efficiency of the module is directly correlated with the TE performance and zT values.^[36] The TaV–NbHf single-leg and uncouple modules, including the TaV–NbHf, NbHf–TaV, NbHf, and TaV modules, were fabricated and tested (Figure 6a and Table S4 (Supporting Information)). Figure 6b,c shows the conversion efficiency (η) of the TaV–NbHf single-leg and uncouple modules as a function of current (I) under different ΔT . The linear relationship of the device voltage (V_d) as a function of I can determine the open voltage (V_{oc}) and internal resistance (R_i) (Figures S13 and S14, Supporting Information). The measured V_{oc} of the modules fits the y intercept of the V_d – I curves well for all five modules. Moreover, V_{oc} and R_i increased with ΔT because of the increase in the Seebeck coefficient and resistivity of the materials. Owing to the significant difference in the cross-sectional areas (A) of the uncouple and single leg, the heat flux (Q_{out}) and the maximum output power (P_{max}) against A (Q_{out}/A and P_{max}/A) were compared. The maximum output powers were ≈ 279 and ≈ 770 mW under ΔT of ≈ 670 K for the TaV–NbHf single-leg and uncouple modules, respectively, when the load resistance was equal to the internal resistance (Figure 6d,e). The maximum conversion efficiency of $\approx 15.2\%$ (TaV–NbHf single leg) and $\approx 13.5\%$ (TaV–NbHf uncouple) was achieved under ΔT of ≈ 670 K, which is high than that of the reported state-of-the-art results.^[8,20,22–24,33–39] The TaV–NbHf and TaV modules exhibit similar efficiencies below $\Delta T = 500$ K, even though the effective zT_{avg} of the TaV–NbHf material was lower than that of the TaV material only. Both theoretical and

experimental results illustrate that the modules using TaV–PIA1123 and NbHf–PIA1123 exhibited lower conversion efficiencies (Figure 6f). This indicates the effectiveness of the resistivity and compatibility matching for conversion efficiency maximization. With a further increase in ΔT , the peak zT of the TaV material was saturated. Thus, the continuous increase in the zT of the NbHf segment dominates the improvement in efficiency. Figure 6f summarizes the conversion efficiencies of all the five modules. Compared to conventional segmented TE modules, such as BiTe/SKD, BiTe/PbTe, and BiTe/hH, a higher conversion efficiency was achieved, even though the zT of the TaV material used for the low-temperature segment was lower than that of the segments (e.g., less than BiTe at < 523 K; less than PbTe at 523 – 873 K). The highest conversion efficiency obtained from the TaV–NbHf single-leg and uncouple modules compared to other configurations (Figure 6a,f) and state-of-the-art results (Figure 1b) strongly verifies the rationality of the synergistical optimization of layered architecture design that significantly improves key aspects, as shown in Figure 2 and Section S1 (Supporting Information). All details of the measured device performances are shown in Figures S13–S17 (Supporting Information), which are consistent with the predicted values. The TaV–NbHf single-leg and uncouple module exhibited good repeatability in multiple tests (Figures S13f and S14f, Supporting Information). Moreover, the scanning electron microscopy (SEM) results of the device at the TaV–NbHf interface after multiple measurement cycles showed that no interdiffusion occurred, further illustrating the good thermal stability at the interface (Figure S18, Supporting Information).

3. Conclusion

In this study, the potential of PIA to simultaneously reduce the lattice thermal conductivity and improve the power factor by grain boundary engineering was demonstrated, resulting in an ultrahigh zT value in (Nb, Hf)FeSb hH alloys. The Sb-vacancy defects attribute mainly to the low lattice thermal conductivity. The well-controlled grain growth with reduced grain boundaries leads to the reduction of electron resistance and the micro-strain is slightly released at grain boundaries. In addition, the well-aligned grain boundaries at the interface of TaV and NbHf materials exhibit no local plastic strain and thereby lead to negligible electrical contact resistance. Compared to conventional segmented TE devices, the synergistical optimization of layered architecture design on hH materials provides a solution for the resistivity and compatibility mismatch among different material systems and reduces contact resistance by avoiding heterogeneous interfaces. As a result, a high-performance TE module with a conversion efficiency of up to $\approx 15.2\%$ was realized. The higher annealing temperature (150–300 K) than the operational hot side and TaV–NbHf interface temperatures of the module ensures the equilibrium state of the materials and interface, thereby achieving stable materials and TE module. These results illustrate that the synergistical optimization of layered architecture design can provide a solution to address the challenges in heterogeneous interfaces, resistivity and compatibility matching, and efficiency maximization to achieve high TE conversion efficiency and application to other TE systems and general devices that require multiparameter matching.

4. Experimental Section

Material Preparation: The p-type (Nb_{0.45}Ta_{0.40}V_{0.10}Ti_{0.05})FeSb and (Nb_{0.88}Hf_{0.12})FeSb materials were synthesized using a high-energy ball milling process. The Nb (99.9%, foil), Ta (99.99%, foil), Ti (99.9%, wire), V (99.99%, piece), Hf (99.9%, piece), Fe (99.995%, piece), and Sb (99.9999%, shot) constituents were weighted in their stoichiometric ratios in a glove box and loaded into a stainless-steel jar. The mixture was ball-milled using a SPEX mixer/mill (Model 8000D, SPEX SamplePrep, Metuchen, NJ, USA) for 20 h to ensure homogeneity. The ground nanopowders were consolidated via spark plasma sintering at 1123 K under a pressure of 80 MPa for 2 min. The detailed TE properties of the (Nb_{0.45}Ta_{0.40}V_{0.10}Ti_{0.05})FeSb are shown in Figure S11 (Supporting Information). The synthesis of the n-type (Hf_{0.6}Zr_{0.4})NiSn_{0.99}Sb_{0.1} with 5 wt% tungsten nanocomposites and its TE properties was introduced in the previous work.^[8]

PIA Process: The consolidated pellets were then polished and placed in a quartz tube. Nb foils were added such that both sides of the pellet were surrounded by Nb foils. The quartz tubes were then sealed under a vacuum of $\approx 10^{-6}$ Torr and annealed at 1073–1123 K for three days.

Material Characterization: All samples were well polished before and after annealing for the characterization of the bulk properties. The electrical conductivity and Seebeck coefficient were measured simultaneously (ULVAC-RIKO ZEM-3 system, Japan) using 2 mm \times 2 mm \times 12 mm bars. The high-temperature thermal properties were determined by measuring the thermal diffusivity using a laser flash system (LFA-467 HT HyperFlash, Germany). Specific heat was measured by differential scanning calorimetry (Netzsch DSC 214, Germany). The thermal conductivity κ was calculated by

$$\kappa = \alpha \rho C_p \quad (8)$$

where α , ρ , and C_p are the thermal diffusivity, density, and specific heat, respectively. The density was measured using the Archimedes' method.

The uncertainties in electrical conductivity, thermal conductivity, Seebeck coefficient, and zT were determined to be $\pm 5\%$, $\pm 2\%$, $\pm 5\%$, and $\pm 7\%$, respectively. The microstructures of the alloys and uncouple module junctions were characterized by field emission scanning electron microscopy (FEI Verios G4), energy dispersive spectroscopy (EDS, Oxford Aztec), and EBSD (FEI Apero S). The grain size and grain boundary distribution were analyzed using an Oxford Aztec Crystal and phase structure was analyzed by TruPhase function. The carrier density and mobility were measured using a LakeShore Hall Effect System (8400 Series HMS, LakeShore). The TEM samples were prepared using a focused ion beam (Scios 2, Thermo Scientific) with a thickness of ≈ 50 nm and analyzed using an FEI Titan G2.

Module Fabrication and Testing: The uncoupled hH module was fabricated using n-type (Hf_{0.6}Zr_{0.4})NiSn_{0.99}Sb_{0.1} with 5 wt% tungsten nanocomposite compounds^[8] and p-type (Nb_{0.45}Ta_{0.40}V_{0.10}Ti_{0.05})FeSb (denoted as TaV-single), (Nb_{0.88}Hf_{0.12})FeSb (denoted as NbHf-single), (Nb_{0.45}Ta_{0.40}V_{0.10}Ti_{0.05})FeSb (low-temperature segment) + (Nb_{0.88}Hf_{0.12})FeSb (high-temperature segment) (denoted as TaV–NbHf), and (Nb_{0.88}Hf_{0.12})FeSb (low-temperature segment) + (Nb_{0.45}Ta_{0.40}V_{0.10}Ti_{0.05})FeSb (high-temperature segment) (denoted as NbHf–TaV). The single-leg test used a 1.84 \times 1.84 \times 5.0 mm³ TaV–NbHf sample. The uncouple modules used leg dimensions of 2.2 \times 2.2 \times 5.0 mm³ for n-type and 2 \times 2 \times 5.0 mm³ for p-type materials. The n- and p-type hH legs were connected electrically in series and thermally in parallel by direct-bond copper substrates using eutectic liquid metal. The module was tested under a vacuum of 10^{-6} Torr.^[58] Graphite foil, silver paste, and thermal paste were used between the TE uncouple module, heat exchanger, and Q-meter to minimize the thermal loss at the interfaces.^[21] The detailed procedure is provided in the previous work.^[24] The schematic of the single-leg measurement is shown in Figure S18 (Supporting Information). The maximum P_{out} (P_{max}), which is the maximum power output from the TE modules, was calculated as follows

$$P_{max} = \frac{V_{oc}^2}{4R_i} \quad (9)$$

where V_{oc} is the measured open-circuit voltage, and R_i is the module internal resistance. Q_{out} is the heat flow to the heat sink, which was given as

$$Q_{out} = \kappa \times A \times \left(\frac{dT}{dx} \right) \quad (10)$$

where κ , A , and dT/dx are the thermal conductivity of the Q-meter, cross-sectional area of the Q-meter, and slope of the temperature difference versus distance on the Q-meter, respectively. The conversion efficiency of the modules considering radiation loss was obtained by^[24]

$$\eta = \frac{P_{out}}{Q_{in}} = \frac{P_{out}}{Q_{out} + P_{out}} \quad (11)$$

where Q_{in} is the heat flow from the heat source. Under the well calibration, the uncertainty of the conversion efficiency measurement was 5–10%. A larger temperature gradient tended to decrease the uncertainty. This uncertainty range was similar to that in existing reports.^[59]

Numerical Modeling: The governing equations describing the TE effect in TEGs were given as^[60–62]

$$\nabla(\kappa \nabla T) + \frac{J^2}{\sigma} - \nabla \cdot \left[\left(\frac{\partial S}{\partial T} \right) \nabla T + (\nabla S)_T \right] = 0 \quad (12)$$

$$\nabla \cdot J = 0 \quad (13)$$

$$J = -\sigma(\nabla V + S \nabla T) \quad (14)$$

where T is the temperature; κ , σ , and S are the temperature-dependent thermal conductivity, electrical conductivity, and Seebeck coefficient, respectively; vector J is the current density; and V is the electrostatic potential. The commercial finite element code COMSOL Multiphysics was used for the numerical simulations. The numerical model was

validated using experimental data before performing the parametric analysis. All temperature-dependent material properties used in the model were obtained from the experimental measurements.

Supporting Information

Supporting Information is available from the Wiley Online Library or from the author.

Acknowledgements

W.L. and B.P. acknowledge the primary financial support from the Army RIF program, which is mainly responsible for this work. The acknowledgements on these secondary supports include: R.A.K. acknowledges the support from the National Renewable Energy Laboratory, operated by the Alliance for Sustainable Energy, LLC, for the U.S. Department of Energy (DOE) under Contract No. DE-AC36-08GO28308. N.L. acknowledges the support from the SBIR program through Nextgen. A.N. acknowledges the financial support from the Office of Naval Research through Grant No. N00014-20-1-2602. Y.Z. acknowledges the support from the SBIR program NanoOhmics. S.P. acknowledges financial support from the NSF CREST program.

Conflict of Interest

The authors declare no conflict of interest.

Data Availability Statement

The data that support the findings of this study are available from the corresponding author upon reasonable request.

Keywords

conversion efficiency, half-Heusler alloy, layered materials, pressure-induced annealing, synergistical optimization, thermoelectric

Received: November 9, 2022

Revised: February 7, 2023

Published online: March 31, 2023

- [1] D. Champier, *Energy Convers. Manage.* **2017**, *140*, 167.
- [2] G. J. Snyder, E. S. Toberer, *Nat. Mater.* **2008**, *7*, 105.
- [3] B. Poudel, Q. Hao, Y. Ma, Y. C. Lan, A. Minnich, B. Yu, X. A. Yan, D. Z. Wang, A. Muto, D. Vashaee, X. Y. Chen, J. M. Liu, M. S. Dresselhaus, G. Chen, Z. F. Ren, *Science* **2008**, *320*, 634.
- [4] W. Li, J. Wang, Y. Xie, J. L. Gray, J. J. Heremans, H. B. Kang, B. Poudel, S. T. Huxtable, S. Priya, *Chem. Mater.* **2019**, *31*, 862.
- [5] W. Y. Zhao, Z. Y. Liu, Z. G. Sun, Q. J. Zhang, P. Wei, X. Mu, H. Y. Zhou, C. C. Li, S. F. Ma, D. Q. He, P. X. Ji, W. T. Zhu, X. L. Nie, X. L. Su, X. F. Tang, B. G. Shen, X. L. Dong, J. H. Yang, Y. Liu, J. Shi, *Nature* **2017**, *549*, 247.
- [6] G. J. Tan, F. Y. Shi, S. Q. Hao, L. D. Zhao, H. Chi, X. M. Zhang, C. Uher, C. Wolverton, V. P. Dravid, M. G. Kanatzidis, *Nat. Commun.* **2016**, *7*, 12167.
- [7] G. J. Tan, X. M. Zhang, S. Q. Hao, H. Chi, T. P. Bailey, X. L. Su, C. Uher, V. P. Dravid, C. Wolverton, M. G. Kanatzidis, *ACS Appl. Mater. Interfaces* **2019**, *11*, 9197.
- [8] H. B. Kang, B. Poudel, W. Li, H. Lee, U. Saparamadu, A. Nozariasbmarz, M. G. Kang, A. Gupta, J. J. Heremans, S. Priya, *Mater. Today* **2020**, *36*, 63.
- [9] S. J. Poon, D. Wu, S. Zhu, W. J. Xie, T. M. Tritt, P. Thomas, R. Venkatasubramanian, *J. Mater. Res.* **2011**, *26*, 2795.
- [10] W. Li, J. Wang, B. Poudel, H. B. Kang, S. Huxtable, A. Nozariasbmarz, U. Saparamadu, S. Priya, *ACS Appl. Mater. Interfaces* **2019**, *11*, 42131.
- [11] Y. Y. Wang, N. S. Rogado, R. J. Cava, N. P. Ong, *Nature* **2003**, *423*, 425.
- [12] H. Zhu, J. Mao, Y. Li, J. Sun, Y. Wang, Q. Zhu, G. Li, Q. Song, J. Zhou, Y. Fu, R. He, T. Tong, Z. Liu, W. Ren, L. You, Z. Wang, J. Luo, A. Sotnikov, J. Bao, K. Nielsch, G. Chen, D. J. Singh, Z. Ren, *Nat. Commun.* **2019**, *10*, 270.
- [13] J. J. Yu, C. G. Fu, Y. T. Liu, K. Y. Xia, U. Aydemir, T. C. Chasapis, G. J. Snyder, X. B. Zhao, T. J. Zhu, *Adv. Energy Mater.* **2018**, *8*, 1701313.
- [14] H. B. Kang, U. Saparamadu, A. Nozariasbmarz, W. Li, B. Poudel, H. Zhu, S. Priya, *ACS Appl. Mater. Interfaces* **2020**, *12*, 36706.
- [15] W. Silpawilawan, K. Kurosaki, Y. Ohishi, H. Muta, S. Yamanaka, *J. Mater. Chem. C* **2017**, *5*, 6677.
- [16] G. Rogl, A. Grytsiv, M. Gurth, A. Tavassoli, C. Ebner, A. Wunschek, S. Puchegger, V. Soprunyuk, W. Schranz, E. Bauer, H. Müller, M. Zehetbauer, P. Rogl, *Acta Mater.* **2016**, *107*, 178.
- [17] C. G. Fu, T. J. Zhu, Y. Z. Pei, H. H. Xie, H. Wang, G. J. Snyder, Y. Liu, Y. T. Liu, X. B. Zhao, *Adv. Energy Mater.* **2014**, *4*, 1400600.
- [18] C. G. Fu, H. J. Wu, Y. T. Liu, J. Q. He, X. B. Zhao, T. J. Zhu, *Adv. Sci.* **2016**, *3*, 1600035.
- [19] A. Nozariasbmarz, U. Saparamadu, W. J. Li, H. B. Kang, C. Dettor, H. T. Zhu, B. Poudel, S. Priya, *J. Power Sources* **2021**, *493*, 229695.
- [20] Y. F. Xing, R. H. Liu, J. C. Liao, Q. H. Zhang, X. G. Xia, C. Wang, H. Huang, J. Chu, M. Gu, T. J. Zhu, C. X. Zhu, F. F. Xu, D. X. Yao, Y. P. Zeng, S. Q. Bai, C. Uher, L. D. Chen, *Energy Environ. Sci.* **2019**, *12*, 3390.
- [21] W. Li, A. Nozariasbmarz, R. A. Kishore, H. B. Kang, C. Dettor, H. Zhu, B. Poudel, S. Priya, *ACS Appl. Mater. Interfaces* **2021**, *13*, 53935.
- [22] X. Hu, P. Jood, M. Ohta, M. Kunii, K. Nagase, H. Nishiate, M. G. Kanatzidis, A. Yamamoto, *Energy Environ. Sci.* **2016**, *9*, 517.
- [23] Q. H. Zhang, J. C. Liao, Y. S. Tang, M. Gu, C. Ming, P. F. Qiu, S. Q. Bai, X. Shi, C. Uher, L. D. Chen, *Energy Environ. Sci.* **2017**, *10*, 956.
- [24] W. Li, B. Poudel, A. Nozariasbmarz, R. Sriramdas, H. Zhu, H. B. Kang, S. Priya, *Adv. Energy Mater.* **2020**, *10*, 2001924.
- [25] G. J. Snyder, T. S. Ursell, *Phys. Rev. Lett.* **2003**, *91*, 148301.
- [26] G. J. Snyder, *Appl. Phys. Lett.* **2004**, *84*, 2436.
- [27] T. Zhu, Y. Liu, C. Fu, J. P. Heremans, J. G. Snyder, X. B. Zhao, *Adv. Mater.* **2017**, *29*, 1605884.
- [28] E. Hazan, O. Ben-Yehuda, N. Madar, Y. Gelbstein, *Adv. Energy Mater.* **2015**, *5*, 1500272.
- [29] C. L. Cramer, H. Wang, M. J. Lance, A. A. Trofimov, E. Cakmak, Z.-H. Jin, *Phys. Status Solidi A* **2022**, *219*, 2100483.
- [30] V. L. Kuznetsov, L. A. Kuznetsova, A. E. Kaliazin, D. M. Rowe, *J. Mater. Sci.* **2002**, *37*, 2893.
- [31] L. J. Xie, H. X. Qin, J. B. Zhu, L. Yin, D. D. Qin, F. K. Guo, W. Cai, Q. Zhang, J. H. Sui, *Adv. Electron. Mater.* **2020**, *6*, 1901178.
- [32] C. Xu, Z. Liang, W. Ren, S. Song, F. Zhang, Z. Ren, *Adv. Energy Mater.* **2022**, *12*, 2202392.
- [33] Y. Xing, R. Liu, J. Liao, C. Wang, Q. Zhang, Q. Song, X. Xia, T. Zhu, S. Bai, L. Chen, *Joule* **2020**, *4*, 2475.
- [34] P. F. Qiu, T. Mao, Z. F. Huang, X. G. Xia, J. C. Liao, M. T. Agne, M. Gu, Q. H. Zhang, D. D. Ren, S. Q. Bai, X. Shi, G. J. Snyder, L. D. Chen, *Joule* **2019**, *3*, 1538.
- [35] G. Nie, W. Li, J. Guo, A. Yamamoto, K. Kimura, X. Zhang, E. B. Isaacs, V. Dravid, C. Wolverton, M. G. Kanatzidis, S. Priya, *Nano Energy* **2019**, *66*, 104193.

- [36] B. B. Jiang, Y. Yu, H. Y. Chen, J. Cui, X. X. Liu, L. Xie, J. Q. He, *Nat. Commun.* **2021**, *12*, 3234.
- [37] Z. Bu, X. Zhang, B. Shan, J. Tang, H. Liu, Z. Chen, S. Lin, W. Li, Y. Pei, *Sci. Adv.* **2021**, *7*, eabf2738.
- [38] M. S. El-Genk, H. H. Saber, T. Caillat, *AIP Conf. Proc.* **2002**, *608*, 1007.
- [39] J. D'Angelo, E. D. Case, N. Matchanov, C. I. Wu, T. P. Hogan, J. Barnard, C. Cauchy, T. Hendricks, M. G. Kanatzidis, *J. Electron. Mater.* **2011**, *40*, 2051.
- [40] C. G. Fu, S. Q. Bai, Y. T. Liu, Y. S. Tang, L. D. Chen, X. B. Zhao, T. J. Zhu, *Nat. Commun.* **2015**, *6*, 8144.
- [41] X. Yan, W. S. Liu, H. Wang, S. Chen, J. Shiomi, K. Esfarjani, H. Z. Wang, D. Z. Wang, G. Chen, Z. F. Ren, *Energy Environ. Sci.* **2012**, *5*, 7543.
- [42] H. Zhu, R. He, J. Mao, Q. Zhu, C. Li, J. Sun, W. Ren, Y. Wang, Z. Liu, Z. Tang, A. Sotnikov, Z. Wang, D. Broido, D. J. Singh, G. Chen, K. Nielsch, Z. Ren, *Nat. Commun.* **2018**, *9*, 2497.
- [43] L. E. Bell, *Phys. Status Solidi A* **2019**, *216*, 1900562.
- [44] P. Ziolkowski, P. Poinas, J. Leszczynski, G. Karpinski, E. Muller, *J. Electron. Mater.* **2010**, *39*, 1934.
- [45] O. Hogblom, R. Andersson, *J. Electron. Mater.* **2014**, *43*, 2247.
- [46] Z. L. Ouyang, D. W. Li, *Sci. Rep.* **2016**, *6*, 24123.
- [47] F. Hao, P. Qiu, Y. Tang, S. Bai, T. Xing, H.-S. Chu, Q. Zhang, P. Lu, T. Zhang, D. Ren, J. Chen, X. Shi, L. Chen, *Energy Environ. Sci.* **2016**, *9*, 3120.
- [48] A. Nozariasbmarz, B. Poudel, W. Li, H. B. Kang, H. Zhu, S. Priya, *iScience* **2020**, *23*, 101340.
- [49] Z. Li, C. Xiao, H. Zhu, Y. Xie, *J. Am. Chem. Soc.* **2016**, *138*, 14810.
- [50] M. Wood, J. J. Kuo, K. Imasato, G. J. Snyder, *Adv. Mater.* **2019**, *31*, 1902337.
- [51] Y. X. Wu, Z. W. Chen, P. F. Nan, F. Xiong, S. Q. Lin, X. Y. Zhang, Y. Chen, L. D. Chen, B. H. Ge, Y. Z. Pei, *Joule* **2019**, *3*, 1276.
- [52] C. J. Zhou, Y. K. Lee, Y. Yu, S. Byun, Z. Z. Luo, H. Lee, B. Z. Ge, Y. L. Lee, X. Q. Chen, J. Y. Lee, O. Cojocar-Miredin, H. Chang, J. Im, S. P. Cho, M. Wuttig, V. P. Dravid, M. G. Kanatzidis, I. Chung, *Nat. Mater.* **2021**, *20*, 1378.
- [53] B. Xu, T. Feng, M. T. Agne, L. Zhou, X. Ruan, G. J. Snyder, Y. Wu, *Angew. Chem., Int. Ed.* **2017**, *56*, 3546.
- [54] J. J. Kuo, S. D. Kang, K. Imasato, H. Tamaki, S. Ohno, T. Kanno, G. J. Snyder, *Energy Environ. Sci.* **2018**, *11*, 429.
- [55] G. J. Snyder, A. H. Snyder, M. Wood, R. Gurunathan, B. H. Snyder, C. N. Niu, *Adv. Mater.* **2020**, *32*, 2001537.
- [56] E. M. Lehigh, Y.-P. Lin, O. E. Lepik, in *Electron Backscatter Diffraction in Materials Science*, (Eds: A. J. Schwartz, M. Kumar, B. L. Adams), Springer US, Boston, MA **2000**, p. 247.
- [57] B. B. Jiang, X. X. Liu, Q. Wang, J. Cui, B. H. Jia, Y. K. Zhu, J. H. Feng, Y. Qiu, M. Gu, Z. H. Ge, J. Q. He, *Energy Environ. Sci.* **2020**, *13*, 579.
- [58] A. Rao, P. Banjade, G. Bosak, B. Joshi, J. Keane, L. Nally, A. Peng, S. Perera, A. Waring, G. Joshi, B. Poudel, *Meas. Sci. Technol.* **2016**, *27*, 105008.
- [59] Z. L. Bu, X. Y. Zhang, Y. X. Hu, Z. W. Chen, S. Q. Lin, W. Li, C. Xiao, Y. Z. Pei, *Nat. Commun.* **2022**, *13*, 237.
- [60] R. A. Kishore, M. Sanghadasa, S. Priya, *Sci. Rep.* **2017**, *7*, 16746.
- [61] R. A. Kishore, A. Nozariasbmarz, B. Poudel, S. Priya, *ACS Appl. Mater. Interfaces* **2020**, *12*, 10389.
- [62] R. A. Kishore, A. Nozariasbmarz, B. Poudel, M. Sanghadasa, S. Priya, *Nat. Commun.* **2019**, *10*, 1765.